Energy & Environmental Science

Accepted Manuscript

ROYAL SOCIETY OF CHEMISTRY

www.rsc.org/ees

Energy & Environmental Science

COMMUNICATION

Micron-Sized Fe-Cu-Si Ternary Composite Anodes for High Energy Li-ion Batteries†

Sujong Chae‡, Minseong Ko‡, Seungkyu Park, Namhyung Kim, Jiyoung Ma and Jaephil Cho*

Received 00th January 20xx,
Accepted 00th January 20xx

DOI: 10.1039/x0xx00000x

www.rsc.org/ees

Nano-engineering of silicon anodes has contributed to demonstrating a promising potential for high energy lithium ion batteries through addressing degradation of battery performances derived from severe volume changes during cycling. However, practical use of nano-engineered silicon anodes still has been stuck because of remaining challenges, such as low tap density, poor scalability and inferior electrical properties. Herein, we successfully developed new Fe-Cu-Si ternary composite (FeCuSi) by scalable spray drying and facile heat treatment. As a result, FeCuSi exhibited remarkable initial Coulombic efficiency (91%) and specific capacity (1287 mAh/g). In order to exactly characterize electrical properties of FeCuSi and directly compare them with industrially developed benchmarking samples, such as silicon monoxide (SiO) and silicon-metal alloy (Si_2Fe), both of half-cell and full-cell test were performed with high electrode density (1.6 g/cc) and high areal capacity (3.4 mAh/cm^2). Overall, FeCuSi showed outperformed discharge capacity and capacity retention in high mass loading for 300 cycles over benchmarking samples.

Broader context

In order to realize the high energy LIBs, extensive studies for the silicon (Si) anode have been carried out for recent years owing to its high gravimetric (3579 mAh/g) and volumetric capacities (2190 mAh/cm^3). Although the advancement in the technology of Si anode has overcome the challenge of Si, such as huge volume change (>300%) during charging and discharging, the Si anode is still far from practical application due to low tap density, poor scalability and inferior electrical properties. In order to move a step closer to using the Si anode for the high energy LIBs, here, we present micron-sized Fe-Cu-Si ternary composite (FeCuSi). FeCuSi has a porous silicon secondary structure where numerous nano-sized metal silicides were embedded. In this design, the porous secondary structure effectively accommodated volume expansion of Si and increased the tap density while accompanying the merits of nano-sized Si for strain and stress relief. Furthermore, the metal silicides reduced interparticle contact resistance and improved structural stability simultaneously with their high electrical conductivities and electrochemical inactivity. The integration of nano-sized Si, metal silicides, and enough void spaces into secondary structure presents a great potential for high capacity anode materials.

To meet urged energy demands for practical applications in portable electronics and electric vehicles, developing electrode materials with high energy density for lithium ion batteries (LIBs) has become a significant research topic.[1-3] On this account, silicon (Si) has been well known for the most promising alternative material as a next-generation LIB anode[4-6] owing to its high gravimetric capacity (3579 mAh/g),[7, 8] low average voltage (~370 mV vs Li/Li$^+$)[4, 9, 10] and its rational production cost.[10, 11] However, its electrochemical performances are drastically deteriorated from electrical isolation and continuous formation of unstable solid electrolyte interphase (SEI) caused by severe volume changes (~400%)[12, 13] during repeated lithium (de)alloying processes.[14, 15] At this point, extensive efforts have succeeded in accommodating volume change through various nano-engineering of Si anodes.[14, 16, 17] However, several challenges of Si nanostructures, such as low tap density, high surface area, and poor electrical properties, have still remained as a practical limitation of LIB applications.[15, 18, 19]

In terms of the industrial approach for improving an energy density of LIBs, Si-graphite blending has been emerged as a practicable method instead of whole utilization of Si-based anodes.[20, 21] Graphite plays a role of improving initial Coulombic efficiency (CE) and maintaining good cycling performance even with small amounts of binding materials (~3%), high electrode density (~1.6 g/cc), and high areal capacity (≥ 3mAh/cm^2). With graphite blending, incorporation of Si and inactive matrix, such as silicon monoxide (SiO_x)[22-25] and Si-metal alloys[26-30], has been attempted vigorously as up-to-date commercialization anode materials. SiO_x has typically 1300-1500 mAh/g of reversible capacity with about 50% of poor initial CE.[22-25] On the other hand, Si-metal alloys, which were synthesized through melt spinning or high-energy mechanical milling process (HEMM), have various reversible capacities (800-1200 mAh/g) and initial CE (80-93%) depending on the kind and proportion of counter metals,

School of Energy and Chemical Engineering, Ulsan National Institute of Science and Technology (UNIST), Ulsan, 689-798, South Korea.
E-mail: jpcho@unist.ac.kr

† Electronic Supplementary Information (ESI) available: The details of the synthetic procedure and characterization methods, Table S1, and Figure S1−S8. See DOI: 10.1039/b000000x/

‡ These authors contributed equally.

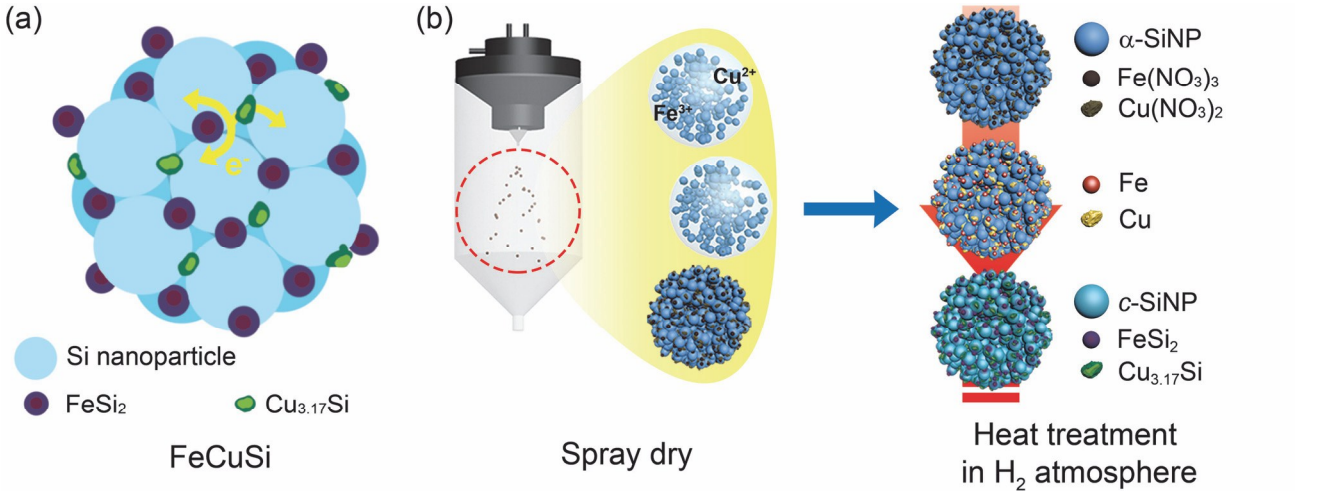

Fig. 1 Schematic illustrations of FeCuSi and its synthesis. (a) Simplified two-dimensional cross-section view of FeCuSi. Silicon nanoparticles build up the secondary particle with metal silicides which can improve electrical conductivity and structural stability. (b) Fabrication process of FeCuSi.

such as Al, Ti, Fe, Ni and etc.[26-30] Both of SiO_x and Si-metal alloys have a common strategy for reducing volume expansion of the electrode via diluting active phases (Si) with inactive phase (Li_4SiO_4[31] and metal silicides[32-34]), resulting in enhancement of electrode stability. However, in spite of graphite blending and their strategies of inactive matrix for addressing the challenges of Si, those are still incompetent materials for alternatives of graphite, because SiO_x has large irreversible capacity loss with low initial CE and Si-metal alloys haven't yet demonstrate stable cycling behaviours in full-cell system, in contrast to showing great cycling performances in a half-cell test. Therefore, it is an important task for battery researchers to develop commercially viable Si-based anodes which have superior battery performances than those of benchmarking samples.

In order to develop the advanced Si material, herein, we present a unique Si secondary structure, Fe-Cu-Si ternary composite (FeCuSi, Fig. 1a), through spray drying and heat treatment. Previously, secondary structures composed of nano-sized Si and carbon have been suggested and demonstrated to decrease surface area and to improve tap density and electrical properties.[18, 19, 35-37] However, previous Si/C secondary structures had a difficulty in achieving high initial CE because the amorphous carbon in secondary structures induced the irreversible capacity losses according to large amounts of trapped lithium ions. In this work, porous Si secondary structures were built up with lithium-inactive metal silicides and Si nanoparticles which were synthesized from monosilane decomposition method from modified CVD process. This distinguished material design brings about multiple fascinating merits. First of all, formation of lithium-inactive metal silicides, such as iron silicide and copper silicide can be easily controlled via simple heat treatment. As a result of decreased amounts of pure Si in the composite, specific capacity can be properly controlled and electrode stability can be improved via decrease of volume change during cycling. Furthermore, metal silicides offer better electrical conductivity,[38, 39] leading to high CE. Secondly, the crystalline Si nanoparticles from the amorphous are expected to not only prevent fracture, owing to its size under the critical fracture size, but also give better electrochemical properties than industrial crystalline Si nanoparticles.[12, 40-42] Thirdly, Si secondary structure accompanies several advantages in common with the previous secondary structure approaches, especially addressing the challenges of nanostructures and alleviating volume change of Si electrode during cycling.[18, 19, 35, 36] Finally, all the fabrication processes including spray drying and simple heat treatment are, moreover, scalable and facile, which are advantageous to cost-effective mass production for commercialization.[35, 43]

The schematic (Fig. 1b) illustrates fabrication procedure of FeCuSi. The amorphous Si nanoparticles prepared by chemical vapor deposition (CVD) process using monosilane at ~400 °C were homogeneously dispersed in distilled water by ultrasonicator. After the dispersion, iron nitrate nonahydrate ($Fe(NO_3)_3{\cdot}9H_2O$) and copper nitrate trihydrate ($Cu(NO_3)_2{\cdot}3H_2O$) were added to the solution as metal precursors. Afterwards, the solution was atomized into microdroplets and dried at 200 °C of inlet temperature through spray dryer. As the droplets evaporated in the spray dryer, the amorphous Si nanoparticles built up spherical type of secondary structure with rational void space. Simultaneously, increased precursor concentration at surface of Si secondary structure leads nano-sized iron nitrate ($Fe(NO_3)_3$) and copper nitrate ($Cu(NO_3)_2$) to be crystallized. Because the concentration and the ratio of the amorphous Si nanoparticle and metal precursors determine drying degree, morphology of secondary structure and the amount of metal silicides, we elaborately optimized the concentration of the precursors as 1.10 wt%, 0.33 wt%, and 0.57 wt% of $Fe(NO_3)_3{\cdot}9H_2O$, $Cu(NO_3)_2{\cdot}3H_2O$, and amorphous Si nanoparticles, respectively. As a result, we successfully obtained the secondary structure with fully dried metal nitrides which were properly adhered in the Si secondary structure.

As a following step, the Si secondary particles, where nano-sized metal nitrates were embedded, were simply heated in hydrogen atmosphere to conduct metal nitrides reduction and metal silicides formation. The reduction from $Fe(NO_3)_3$ and $Cu(NO_3)_2$ to Fe and Cu began in earnest after 200 °C, which was accelerated with raising heating temperature and heating time.[44] As the temperature increased, amorphous Si became crystallized and the reduced metals reacted with Si gradually, leading to formation of iron silicides ($FeSi_2$) and copper silcides ($Cu_{3.17}Si$). It is noted that the heat treatment condition including time and temperature affects the phase transformation of the secondary structure, which is strongly related with electrochemical properties. We finally optimized the heating temperature at 860 °C.

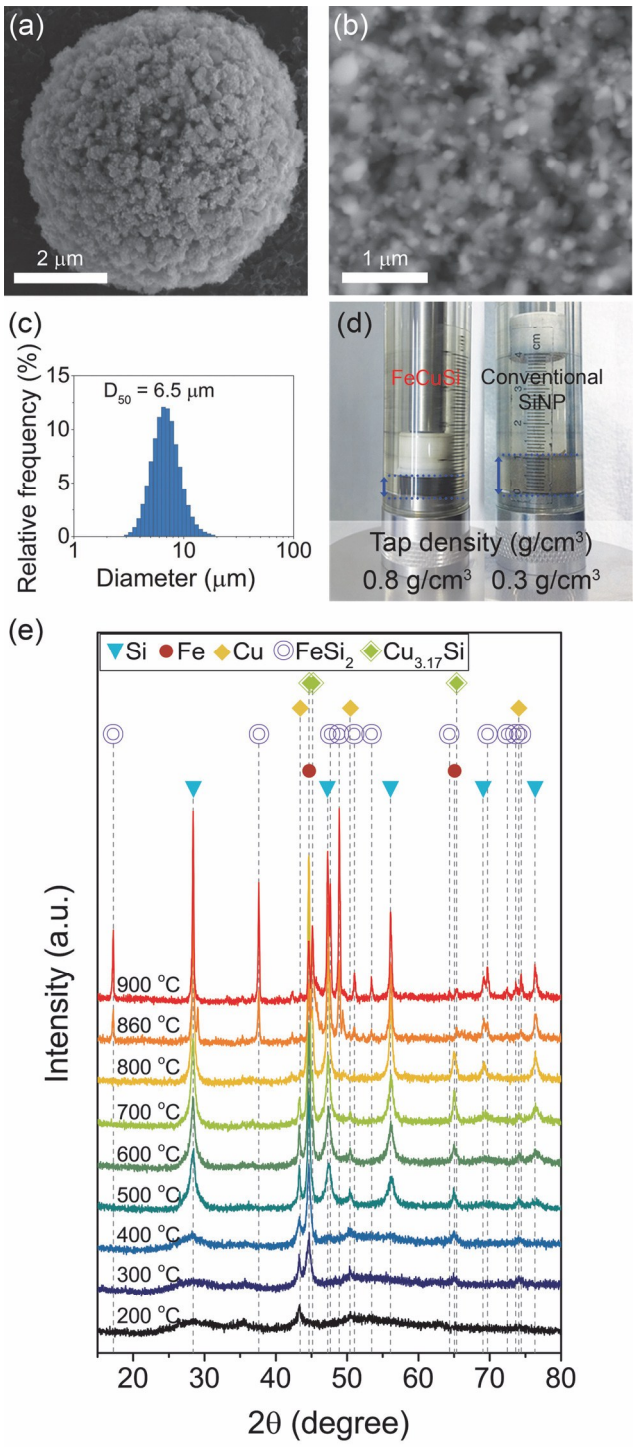

Fig. 2 Characterization of FeCuSi. (a) SEM image of FeCuSi. (b) Magnified cross-sectional SEM images of FeCuSi.(c) Statistical analysis for the size distribution of FeCuSi. (d) Volume comparison between 1 g of FeCuSi and conventional Si nanoparticles after measuring tap density. (e) X-ray diffraction patterns of FeCuSi as a function of heating temperature.

For a detailed material characterization of FeCuSi, we carried out scanning electron microscopy (SEM) with focused ion beam (FIB), the analysis for the size distribution and tap density, Brunauer-Emmett-Teller (BET) analysis, Barrett-Joyner-Halenda (BJH) analysis and X-ray diffraction (XRD) analysis (Fig. 2). As shown in SEM images in top and cross sectional views (Fig. 2a and b), the shape

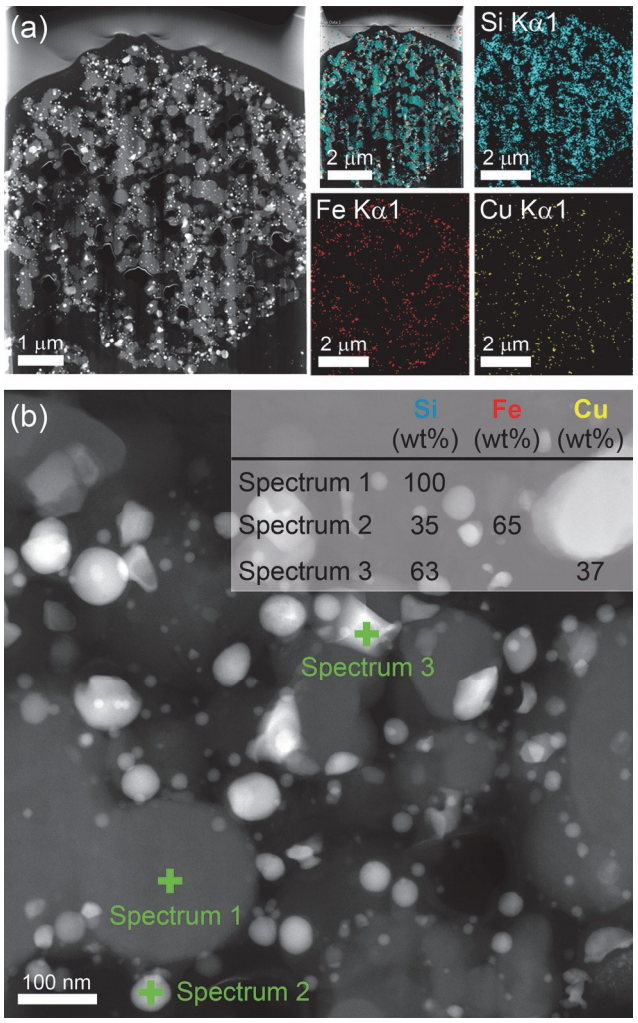

Fig. 3 Detailed investigation of FeCuSi with TEM analysis. (a) HAADF-STEM image and EDS mapping of FeCuSi in cross sectional view. Cyan, red, and yellow indicate Si, Fe, and Cu respectively. (b) Magnified HAADF-STEM image of FeCuSi and EDS point analysis for Si nanoparticle, iron silicide, and copper silicide.

of FeCuSi is spherical secondary structure which is composed of Si primary particles, where metal silicides are adhered, and void space. Owing to the benefits of nano-size of Si, which is less than 150 nm (Fig. S1), lithium-inactive metal silicides and proper void in the structure, FeCuSi can relieve the volume expansion of the composite electrode effectively within its inner void space. The size of FeCuSi varies from 3.0 μm to 18.5 μm with average diameter (D_{50}) of 6.5 μm (Fig. 2c). Besides, the tap density (Fig. 2d) also measured 0.8 g/cm^3 which is much higher than that of commercially available Si nanoparticles with 0.3 g/cm^3. The size and high tap density of FeCuSi are expected to be more favorable to conventional electrode fabrication than nanomaterials owing to homogeneous slurry mixing[45] and increase of volumetric energy density.[18, 19] With BET and BJH analysis, we got the pore size distribution (Fig. S2) and specific surface area as 15.02 m^2/g. XRD pattern (Fig. 2e) shows the phase transformation of FeCuSi with raising heating temperature. The samples for the analysis were prepared by heat treatments with 1 hour of duration time and different heating temperatures from 200 °C to 900 °C. Based on the analysis, the intensities of the peaks pointing to Fe and Cu got increased gradually with raising heating temperature from 200 °C, which clearly indicates that the reduction of $Fe(NO_3)_3$

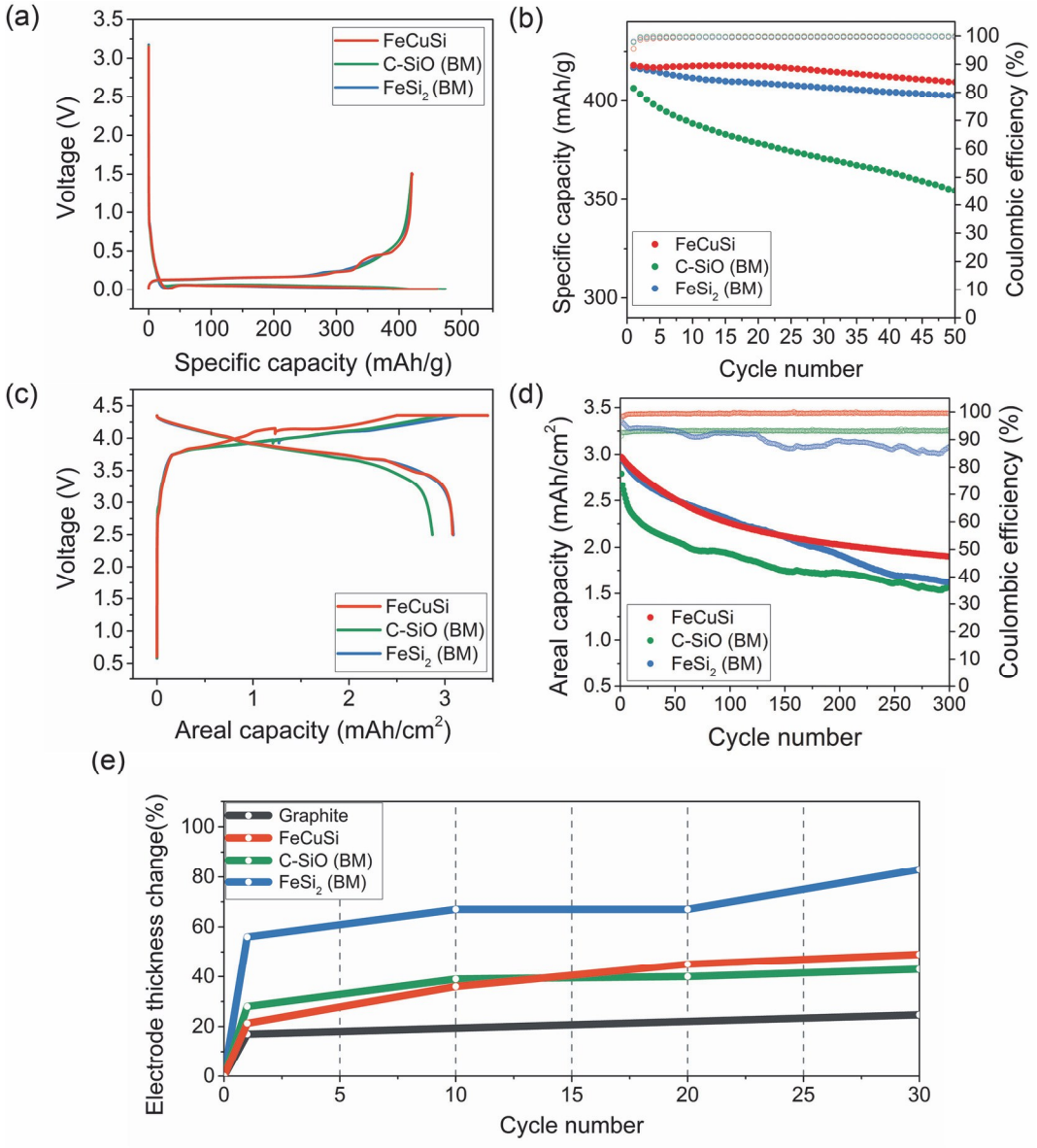

Fig. 4 Electrochemical characterization of FeCuSi anode with benchmarking samples in half-cell (a, b) and full-cell (c, d) and measurement of the thickness change of electrode (e). (a) Voltage profiles of FeCuSi, C-SiO_x, and $FeSi_2$ at the formation cycle. (b) Reversible capacities and cycling CEs of FeCuSi, C-SiO_x, and $FeSi_2$ for 50 cycles. The formation cycle (a) and cycling test (b) in half-cell were carried out at a rate of 0.1C and 0.5C, respectively. (1C = 0.42 A/g.) (c) Voltage profiles of full-cell systems with LCO and different anodes of FeCuSi, C-SiO_x, and $FeSi_2$ at the formation cycle. (d) Reversible capacities and cycling CEs of the full-cells for 300 cycles with 1C. The formation cycle (c) and cycling test (d) in full-cell were carried out at a rate of 0.1C and 1C, respectively. (1C = 3.0 mA/cm^2.) All electrochemical tests were performed at 25 °C in 2032R coin-type cell. (e) The change of electrode thickness of graphite, FeCuSi, C-SiO_x, and $FeSi_2$ at lithiated state during 30 cycles. Electrode thickness at the lithiation state were measured with a micrometer after disassembling coin cells in Ar-filled glove box.

and $Cu(NO_3)_2$ proceeded gradually as temperature increases. In addition, the peaks of Fe and Cu considerably diminished and the peaks of $Cu_{3.17}Si$ and $FeSi_2$ were obviously observed after 800 °C. These metal silicides, which are inactive to lithium,[5] not only make volume change of the composite controllable through decreasing the amount of lithium-active phase but also supply electrical conducting channels[38, 39] between Si nanoparticles. Furthermore, with alloy reaction between silicon and metals, metal silicides reinforced the secondary structure by sticking to the junctions between Si nanoparticles. In addition, we can also observe the structural change of Si from amorphous to crystalline phase. From the Halder-wagner method, we can calculate the crystallite size of Si as a function of temperature (Fig. S3). The optimized FeCuSi which was treated at 860 °C had 30.5 nm of crystallite size. Compared to FeCuSi at 900 °C, the optimized one can be regarded as more effective on mitigating the localization of stress in its structure when electrochemically (de)alloying with lithium.

High resolution transmission electron microscopy (HR-TEM) was performed to investigate the morphology of FeCuSi in detail (Fig. 3). The sample for cross-sectional view was prepared by FIB with epoxy soak and carbon deposition in order to make protective layers in the top and void of the sample against the damage derived from Ga ion beam. As seen in high angle annular dark field in a scanning transmission electron microscope (HAADF-STEM) image (Fig. 3a), the morphology accurately coincides with that of cross sectional SEM image. In addition, it was confirmed through energy-dispersive X-ray spectroscopy (EDS) analysis that Fe (red) and Cu (yellow) elements

Table 1 Summary of electrochemical performance of FeCuSi and benchmarking samples

	Only Si-based anodes		Si-Graphite blending anodes for 420 mAh/g			Full cell with Si-Graphite blending anodes and LCO		
Sample	Specific capacity (mAh/g)	Initial CE (%)	Initial CE (%)	Capacity retention (%, 50th cycle)	Electrode thickness change (%, 30th cycle)	Cell capacity (mAh/cm^2)	Initial CE (%)	Capacity retention (%, 300th cycle)
FeCuSi	1287	91	91.4	98.0	49	3.08	89.4	63.9
C-SiO_x	1673	77	88.5	96.5	43	2.87	85.4	56.2
$FeSi_2$	1148	88	91.1	87.2	83	3.08	89.4	54.6

are extremely well distributed in the Si (cyan) secondary structure. For the sake of the elemental characterization of Fe, Cu, and Si, point analysis was conducted in high magnification (Fig. 3b). It turned out that large circle, small circle, and shapeless one correspond to Si, Fe, and Cu elements, respectively, indicating morphology of metal silicides. Besides, mixed elements detection of Si and Fe at small circle and Si and Cu at shapeless one confirmed the formation of metal silicides. EDS line scan profile also strengthen the basis of coexistence of Fe, Cu, and Si (Fig. S4). Therefore, in sum, as described in HAADF-STEM images and EDS analysis, numerous nano-sized metal silicides were adhered to spherical Si secondary structure evenly for the purpose of improving both structural stability and electrical conductivity.

As an investigation into the effect of our material design on Si anode, electrochemical properties of FeCuSi were evaluated with coin-type lithium half-cell at 24 °C (Fig. S5). FeCuSi exhibited 1287 mAh/g of high specific capacity and 91% of outstanding initial CE at the formation cycle with 0.05C (Fig. S5a). In addition, stable cycling for 50 cycles with 90% of capacity retention was also attained at 0.5C (Fig. S5b). This excellent performance is attributable to the improved electrical conductivity and structural stability owing to decrease of internal resistance from countless nano-sized metal silicides and robust secondary structure with void space. As shown in Fig. S6, the amount of metal silicides which was controlled by the temperature of heat treatment determined both of specific capacity and initial CE, indicating that we successfully found the optimized condition for FeCuSi.

The electrochemical performance of FeCuSi was also evaluated with other industrially developed benchmarking samples (Fig. 4), which are carbon coated silicon monoxide (C-SiO_x) and Si embedded in inactive matrix of iron silicide ($FeSi_2$), in order to see feasibility of the practical application with benchmark comparison. C-SiO_x and $FeSi_2$ exhibited 1673 and 1148 mAh/g of specific capacities with 77% and 88% of initial CE at the formation cycle with 0.05C, respectively (Fig. S5 a). Herein, three samples were blended with graphite in the industrial standard electrode condition in order to be tested in real LIB application, where the electrodes have high areal capacity (3.44 mAh/cm^2) and high electrode density (1.6 g/cc) with minimized addition of binding materials (1.5 % of each styrene butadiene rubber (SBR) and carboxymethyl cellulose (CMC) in slurry). In these electrodes, graphite enables Si anodes to be readily calendered as a lubricant and conducting agent, which consequentially improves energy density of the battery.[5, 21] Each of the electrodes was adjusted to exhibit same specific capacity as ~420 mAh/g by different blending ratios of Si-based materials and graphite, where the blending ratios were 7 wt%, 5 wt% and 9 wt% for FeCuSi, C-SiO_x, and Si_2Fe, respectively. FeCuSi and $FeSi_2$ showed 91.4% and 91.1% of high CEs at the formation cycle with 0.1C, whereas C-SiO_x had 88.5% of relatively low CE (Fig. 4a). In cycling test at a rate of 0.5C, the most stable cycling behavior was achieved in FeCuSi with 98% of capacity retention after 50 cycles (Fig. 4b).

Furthermore, we also performed even full-cell test of three samples with commercialized $LiCoO_2$ as a cathode in the voltage range of 2.5 – 4.35V (Fig. 4c and d). $LiCoO_2$ which we adopted here is considered as qualified reference cathode owing to its very high initial CE and stable cycling behavior (Fig. S7). The ratio of negative to positive charge capacity (*N/P* ratio) was between 1.11 and 1.14 and the areal capacity of cathode was fixed with 3.42 mAh/cm^2 because the excessive raising of loading level of cathode is restricted by the deterioration of battery performances.[46] In the formation cycle, FeCuSi and Si_2Fe exhibited 3.08 mAh/cm^2 of initial areal capacity, however C-SiO_x exhibited only 2.87 mAh/cm^2 of initial areal capacity derived from its low CE (Fig. 4c). Cycling test with a rate of 1C showed that FeCuSi discharged the highest capacity at each cycle during 300 cycles (Fig. 4d) and voltage profiles at 1st, 100th, 200th, and 300th cycle supported the cycling test result (Fig. S8).

To interpret the result of cycling test in full cells, electrode thickness changes of three samples in half-cell cycling at 0.5C were measured at lithiated state (Fig. 4e). Wu et al., reported that the severe volume expansion of Si (~420%) is generally considered as the main reason for the battery failure of Si electrode, such as material pulverization, morphology and volume change of the whole Si electrode, and SEI accumulation. [14] Consequentially, there has been various approaches to prevent those challenges through alleviating the volume expansion of the Si electrode via building nanostructures.[17] In the same vein, the collective behavior of nano-silicon on the electrode during cycling was analyzed by Radvanyi et al., demonstrating the failure mechanisms of nano-silicon anodes with the porosity evolution, electrode thickness change, and SEI accumulation.[47] Among the phenomena indicating the failure mechanisms, more importantly, the electrode thickness change is the result of collective behavior of volume change of each Si material in the electrode. Thus, the measurement of electrode thickness change indicates the macroscopic view of the volume change of Si material. Recently, several reports also supported their battery performances with the electrode thickness change.[40, 48- 50] In this study, the electrode thickness change during cycling (Fig. 4e) can be a simple index for the volume expansion of

the Si electrode and accounting for overall battery failure of Si electrodes in half-cell and full-cell.

The result exhibited that smaller thickness change of FeCuSi than that of $FeSi_2$, owing to Si secondary structure with surplus void, decisively brought about better capacity retention. Especially, the continuous increase in the electrode thickness change of $FeSi_2$ is regarded as one of main causes for capacity degradation during cycling. Although C-SiO_x behaved stable cycling with the lowest electrode thickness change, the discharge capacity at each cycle was smaller than that of FeCuSi because of the large irreversible capacity losses in initial cycles.

In summary, the new approach to solve the challenges of Si anode has been presented via developing Si secondary structure containing void space and numerous nano-sized metal silicides (FeCuSi) with using scalable spray drying and simple heat treatment. With exquisitely developed FeCuSi, both half-cell and full-cell test were carried out with high areal capacity (3.4 mAh/cm^2) and high electrode density (1.6 g/cc) in order to diagnose battery performances precisely. In half-cell test, where the active material was only composed of FeCuSi, 91% of initial CE with 1287 mAh/g of specific capacity was attained at the formation cycle. Besides, contrastive analysis with two of industrially developed benchmarking samples, which were C-SiO_x and $FeSi_2$, represented that FeCuSi exhibited the most stable cycling behavior with 98% of capacity retention after 50th cycle in high mass loading half-cell. Moreover, in terms of full-cell test with LCO, FeCuSi had superior discharge capacity at each cycle during 50th cycles with a high initial CE (89.4%) when compared with other benchmarking samples. Excellent battery performances of FeCuSi are considered as the fruits of the distinctive features which were confirmed by its material characterization: 1) Crystallized Si nanoparticles from amorphous one has several advantages in battery performances; 2) Si secondary structure with void space enable to alleviate volume change during cycling; 3) Abundant nano-sized metal silicides facilitate improvement of electrical conductivity effectively through reducing interparticle resistance; 4) Those metal silicides can not only reinforce the secondary structure as glue between Si particles but also reduce the volume expansion of the composite via diluting lithium-active phase. The accommodation of volume change during cycling was clearly elucidated in measuring electrode thickness change. However, we recognized that the cycling stability in full-cell system, under the condition of high areal capacity and high electrode density, still needs to be improved further via adjusting void space or wrapping Si secondary structure with lithium-conductive and rigid materials such as coal tar pitch. We believed that this advanced secondary structure design with metal silicides, which can alleviate volume change and have a high electrical conductivity, will be feasible candidate of next generation anode for high energy density batteries in the future.

Acknowledgements

This work was supported by the IT R&D program of MOTIE/KEIT (Development of Li-rich Cathode and Carbon-free Anode Materials for High Capacity/High Rate Lithium Secondary Batteries, 10046309).

References

1. N. S. Choi, Z. Chen, S. A. Freunberger, X. Ji, Y. K. Sun, K. Amine, G. Yushin, L. F. Nazar, J. Cho and P. G. Bruce, *Angew Chem Int Ed Engl*, 2012, **51**, 9994-10024.
2. J. Liu, *Adv. Funct. Mater.*, 2013, **23**, 924-928.
3. E. C. Evarts, *Nature*, 2015, **526**, S93-95.
4. C. M. Park, J. H. Kim, H. Kim and H. J. Sohn, *Chem Soc Rev*, 2010, **39**, 3115-3141.
5. M. N. Obrovac and V. L. Chevrier, *Chemical Reviews*, 2014, **114**, 11444-11502
6. X. Su, Q. L. Wu, J. C. Li, X. C. Xiao, A. Lott, W. Q. Lu, B. W. Sheldon and J. Wu, *Adv. Energy Mater.*, 2014, **4**, 1300882.
7. M. N. Obrovac and L. Christensen, *Electrochem Solid St*, 2004, **7**, A93-A96.
8. M. N. Obrovac and L. J. Krause, *J. Electrochem. Soc.*, 2007, **154**, A103-A108.
9. W. J. Zhang, *J. Power Sources*, 2011, **196**, 13-24.
10. N. Nitta and G. Yushin, *Particle & Particle Systems Characterization*, 2014, **31**, 317-336.
11. L. Ghadbeigi, J. K. Harada, B. R. Lettiere and T. D. Sparks, *Energy Environ. Sci.*, 2015, **8**, 1640-1650.
12. M. T. McDowell, S. W. Lee, J. T. Harris, B. A. Korgel, C. Wang, W. D. Nix and Y. Cui, *Nano Lett*, 2013, **13**, 758-764.
13. M. T. McDowell, S. W. Lee, W. D. Nix and Y. Cui, *Adv Mater*, 2013, **25**, 4966-4985.
14. H. Wu and Y. Cui, *Nano Today*, 2012, **7**, 414-429.
15. M. Ko, P. Oh, S. Chae, W. Cho and J. Cho, *Small*, 2015, **11**, 4058-4073.
16. J. R. Szczech and S. Jin, *Energy Environ Sci*, 2011, **4**, 56-72.
17. M. Ko, S. Chae and J. Cho, *Chemelectrochem*, 2015, **2**, 1645-1651.
18. N. Liu, Z. D. Lu, J. Zhao, M. T. McDowell, H. W. Lee, W. T. Zhao and Y. Cui, *Nat Nanotechnol*, 2014, **9**, 187-192.
19. D. C. Lin, Z. D. Lu, P. C. Hsu, H. R. Lee, N. Liu, J. Zhao, H. T. Wang, C. Liu and Y. Cui, *Energy Environ Sci*, 2015, **8**, 2371-2376.
20. N. Dimov, Y. Xia and M. Yoshio, *J. Power Sources*, 2007, **171**, 886-893.
21. Z. Du, R. A. Dunlap and M. N. Obrovac, *J Electrochem Soc*, 2014, **161**, A1698-A1705.
22. J. Yang, Y. Takeda, N. Imanishi, C. Capiglia, J. Y. Xie and O. Yamamoto, *Solid State Ionics*, 2002, **152**, 125-129.
23. T. Kim, S. Park and S. M. Oh, *J. Electrochem. Soc.*, 2007, **154**, A1112-A1117.
24. C. M. Park, W. Choi, Y. Hwa, J. H. Kim, G. Jeong and H. J. Sohn, *J. Mater. Chem.*, 2010, **20**, 4854-4860.
25. J. H. Kim, C. M. Park, H. Kim, Y. J. Kim and H. J. Sohn, *J Electroanal Chem*, 2011, **661**, 245-249.
26. M.-S. Park, S. Rajendran, Y.-M. Kang, K.-S. Han, Y.-S. Han and J.-Y. Lee, *J. Power Sources*, 2006, **158**, 650-653.
27. H. Jung, Y. U. Kim, M. S. Sung, Y. Hwa, G. Jeong, G. B. Kim and H. J. Sohn, *J. Mater. Chem.*, 2011, **21**, 11213-11216.
28. S. B. Son, S. C. Kim, C. S. Kang, T. A. Yersak, Y. C. Kim, C. G. Lee, S. H. Moon, J. S. Cho, J. T. Moon, K. H. Oh and S. H. Lee, *Adv. Energy Mater.*, 2012, **2**, 1226-1231.
29. K. J. Lee, S. H. Yu, J. J. Kim, D. H. Lee, J. Park, S. S. Suh, J. S. Cho and Y. E. Sung, *J. Power Sources*, 2014, **246**, 729-735.
30. T. Song, K. C. Kil, Y. Jeon, S. Lee, W. C. Shin, B. Chung, K. Kwon and U. Paik, *J. Power Sources*, 2014, **253**, 282-286.

31. M. A. Al-Maghrabi, J. Suzuki, R. J. Sanderson, V. L. Chevrier, R. A. Dunlap and J. R. Dahn, *J. Electrochem. Soc.*, 2013, **160**, A1587-A1593.
32. W. J. Weydanz, M. Wohlfahrt-Mehrens and R. A. Huggins, *J. Power Sources*, 1999, **81-82**, 237-242.
33. A. Netz, R. A. Huggins and W. Weppner, *J. Power Sources*, 2003, **119**, 95-100.
34. A. Netz and R. A. Huggins, *Solid State Ionics*, 2004, **175**, 215-219.
35. D. S. Jung, T. H. Hwang, S. B. Park and J. W. Choi, *Nano Lett*, 2013, **13**, 2092-2097.
36. S. D. Xun, B. Xiang, A. Minor, V. Battaglia and G. Liu, *J. Electrochem. Soc.*, 2013, **160**, A1380-A1383.
37. S. Choi, D. S. Jung and J. W. Choi, *Nano Lett*, 2014, **14**, 7120-7125.
38. P. Wang, Y. NuLi, J. Yang and Y. Zheng, *Int J Electrochem Sc*, 2006, **1**, 122-129.
39. H. Usui, K. Meabara, K. Nakai and H. Sakaguchi, *Int J Electrochem Sc*, 2011, **6**, 2246-2254.
40. M. Ko, S. Chae, S. Jeong, P. Oh and J. Cho, *Acs Nano*, 2014, **8**, 8591-8599.
41. X. H. Liu, L. Zhong, S. Huang, S. X. Mao, T. Zhu and J. Y. Huang, *ACS Nano*, 2012, **6**, 1522-1531.
42. A. S. Fedorov, Z. I. Popov, A. A. Kuzubov and S. G. Ovchinnikov, *Jetp Lett.*, 2012, **95**, 143-147.
43. A. Carne-Sanchez, I. Imaz, M. Cano-Sarabia and D. Maspoch, *Nat Chem*, 2013, **5**, 203-211.
44. S. Yuvaraj, F. Y. Lin, T. H. Chang and C. T. Yeh, *J Phys Chem B*, 2003, **107**, 1044-1047.
45. V. A. Atiemo-Obeng, W. R. Penney and P. Armenante, in *Handbook of Industrial Mixing*, John Wiley & Sons, Inc., 2004, ch10, pp. 543-584.
46. H. H. Zheng, J. Li, X. Y. Song, G. Liu and V. S. Battaglia, *Electrochim. Acta*, 2012, **71**, 258-265.
47. E. Radvanyi, W. Porcher, E. De Vito, A. Montani, S. Franger and S. Jouanneau Si Larbi, *Phys Chem Chem Phys*, 2014, **16**, 17142-17153.
48. R. Yi, F. Dai, M. L. Gordin, S. R. Chen and D. H. Wang, *Adv. Energy Mater.*, 2013, **3**, 295-300.
49. C. Kim, M. Ko, S. Yoo, S. Chae, S. Choi, E.-H. Lee, S. Ko, S.-Y. Lee, J. Cho and S. Park, *Nanoscale*, 2014, **6**, 10604-10610.
50. Z. Lu, N. Liu, H.-W. Lee, J. Zhao, W. Li, Y. Li and Y. Cui, *Acs Nano*, 2015, **9**, 2540-2547.

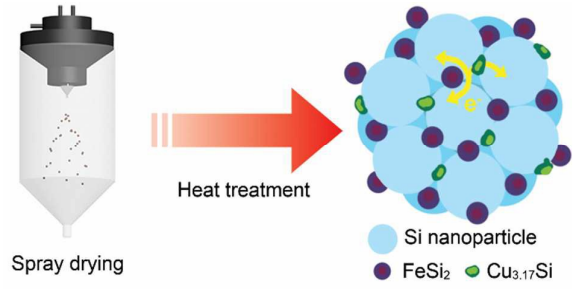

Table of contents

To develop the practicable Si-based anode for high-energy LIBs, the FeCuSi composite was developed with properly building Si-metal alloys.